

MODELING OF INDIRECT-DRIVE ICF IMPLOSIONS USING 1D HYDRODYNAMIC CODE WITH INLINE COLLISIONAL-RADIATIVE ATOMIC KINETICS.

I. E. Golovkin¹, J. J. MacFarlane¹, P. R. Woodruff¹,
L. A. Welser², D. L. McCrorey², R. C. Mancini², J. A. Koch³

¹ Prism Computational Sciences, Madison, WI 53711
e-mail: golovkin@prism-cs.com

² University of Nevada, Reno, NV 89557

³ Lawrence Livermore National Laboratory, CA 94550

K-shell emission spectroscopy is commonly used to diagnose the core temperature and density of Ar-doped ICF implosions at OMEGA and Z. To investigate details of spectra formation and energy transport, we perform simulations of Ar-doped indirect laser-driven implosions. We use VisRad, a user-friendly view factor code that simulates the radiation environment in three-dimensional objects, to predict the temperature and radiative flux distributions throughout target components in high-power laser and z-pinch laboratory plasma experiments. Time-dependent hohlraum radiation temperatures and fluxes, computed with VisRad, are used to initialize target implosion simulations with the 1D radiation-hydrodynamics code, HELIOS. This code includes inline collisional-radiative atomic kinetics and multi-angle short-characteristics radiation transport. In particular, we address the impact of Ar line radiation on implosion dynamics. We will also address the importance of time-dependent atomic kinetics for ionization distribution and spectra formation. We discuss details of the calculations and compare our results with experimental data.

I. INTRODUCTION.

Recently, a set of experiments at the OMEGA laser facility has been performed in order to infer plasma temperature and density distributions at the collapse of an ICF implosion by simultaneously recording time-resolved spectra and monochromatic images^{1,2}. These experiments provide valuable information for benchmarking and validating radiation-hydrodynamics codes. In this paper, we will report on the results of 1-D hydro simulations, with a particular emphasis on accurate accounting for atomic kinetics and radiation transport.

In these indirect-drive experiments, thirty laser beams were used to deliver a total of 15 kJ of energy to the hohlraum, in a 1-ns square laser pulse. The beam pointing was chosen to achieve a high degree of radiation uniformity on the target surface. In order to calculate time-, and frequency-dependent radiation flux on the target surface, we utilize *VisRad*³. This 3D view factor code computes fluxes and radiation temperatures using characteristic laser beam profile parameters, hohlraum albedos and x-ray conversion coefficients. We estimate peak radiation temperature at the target surface to be ~190 eV, with small variations from the equatorial plane to the poles of the target.

This radiation flux information is used to drive the implosion calculation. The targets are 220 μm inner radius, plastic, micro-balloons with a 35 μm wall thickness, filled with 50 atm. DD and 0.1 atm. Ar. Hydro simulations were performed using the 1D Lagrangian code *HELIOS* with an inline collisional-radiative module. Conventionally, hydro codes employ diffusion algorithms and LTE multi-group opacities to compute radiation transport in plasmas. For these systems, however, this approximation may not be valid since the plasma is not diffusive and not necessarily in LTE. It is known, that even in small quantities, Ar line radiation contributes significantly to plasma cooling. In order to carefully quantify this effect, we use time-dependent atomic kinetics with multi-angle short-characteristics radiation transport inline with the hydro. At every hydro time step, NLTE populations and the radiation field are computed and used to calculate plasma cooling and heating rates. This allows us to treat energy transport in plasma with a high level of accuracy.

The argon atomic model includes ground and singly excited states up to $n=6$ for each ionization stage, since a vast variety of temperatures and

densities is expected while the system goes from its initial state through implosion to the stagnation phase. Satellites to $\text{Ly}\alpha$ and $\text{He}\alpha$ lines (with spectator electrons in $n=2$) are also considered, because they may affect K-shell emission and population distributions at stagnation. Calculations include the effects of bound-bound, bound-free, and free-free contributions to the plasma emission and opacity. Atomic processes include electron collisional ionization, recombination, excitation, and deexcitation; spontaneous emission; radiative recombination; autoionization, electron capture, dielectronic recombination, photoionization and photoexcitation. Lineshapes include the effects of natural, Doppler and Stark broadening. All energy level structures, rates, and cross-sections are computed with the code *ATBASE*. *HELIOS* utilizes a two-temperature plasma model ($T_e \neq T_i$), and *SESAME* equations of state.

We then post-process the plasma temperature and density distributions around the time of implosion stagnation, as obtained from the hydro code, with a multi-dimensional spectral package *SPECT3D*. The atomic model for Ar is more comprehensive in this case, since we are interested in the details of spectral formation, and not just energy transport in plasmas. The spectral region of interest ranges from 3000 to 4500 eV, which covers all relevant Ar K-shell emission lines. We include He and Li-like satellite transitions to the Ly and He lines (α through γ) with the spectator electrons in $n \leq 4$. To illustrate the effects of time-dependent atomic kinetics on the formation of spectral features and the ionization balance, we performed a set of single cell calculations with the code *PrismSPECT* at the plasma conditions characteristic of peak temperature (at the collapse of the main shock wave), and peak density (stagnation).

In the next section, we will discuss the results of the simulations.

II. RESULTS.

An accurate prediction of radiation drive flux is crucial for indirect-drive implosion simulations. Hohlraum dimensions and orientation, and laser parameters are based on experimental conditions². *VisRad* estimates the peak radiation temperature at the target surface to be $\sim 190\text{eV}$, which drops at the end of the laser pulse. *VisRad* predictions are benchmarked against experimentally measured hohlraum temperatures for similar conditions⁴.

The targets are 220 μm inner radius plastic micro-balloons with a 35 μm wall thickness filled with 50 atm. DD. In the calculations, we vary the Ar

concentration, so that we can study the effects of Ar line emission on the energy transport. Figure 1 illustrates hydro zone boundary positions as a function of time, along with the radiation drive temperature for the 0.1 atm Ar filling pressure. The time of the peak plasma temperature, associated with the collapse of the main shock wave, agrees well with the experimentally measured peak neutron flux (1.5 – 1.6 ns with respect to the leading edge of the laser pulse). Peak compression occurs approximately 200 ps later.

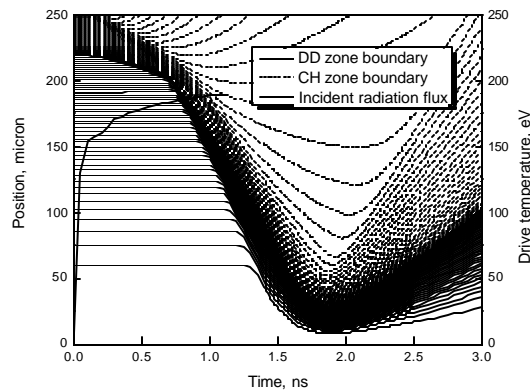


Figure 1. RT diagram of implosion calculation driven with $\sim 190\text{eV}$ radiation.

Temporal evolution of temperature and density for several Lagrangian fluid elements is displayed in Figure 2. Zone 1 represents the target center, and zone 50 the last fuel zone interfacing the pusher. Computed plasma conditions agree well with the temperature and density distributions obtained from the analysis of experimental data. The temperature in the experiment peaks at 1000 eV at the center, and drops smoothly to 500 eV towards the core edge. The electron density stays at $1.2 \times 10^{24} \text{ cm}^{-3}$ rising sharply to $1.6 \times 10^{24} \text{ cm}^{-3}$ at the fuel-pusher interface. Calculated plasma conditions lie well within uncertainty intervals of the analysis. Experimental values for temperature and density gradients in the core were obtained using simultaneous fitting⁵ of time-integrated Ar emission spectra and monochromatic images. Therefore, they represent the plasma distributions effectively averaged over the duration of Ar emission. The details of the experimental data analysis are currently being prepared for publication⁶.

To show the importance of Ar line emission on the overall energy balance in the plasma, we performed a set of calculations varying the Ar concentration. The simulations were done with pure DD, 0.1, and 0.5 atm initial Ar filling pressure. Figure 3 clearly indicates the effect of Ar emission. The

higher the concentration of Ar, the greater is the amount of energy loss by the core. This results, in turn, in lower core pressure, and therefore higher compression.

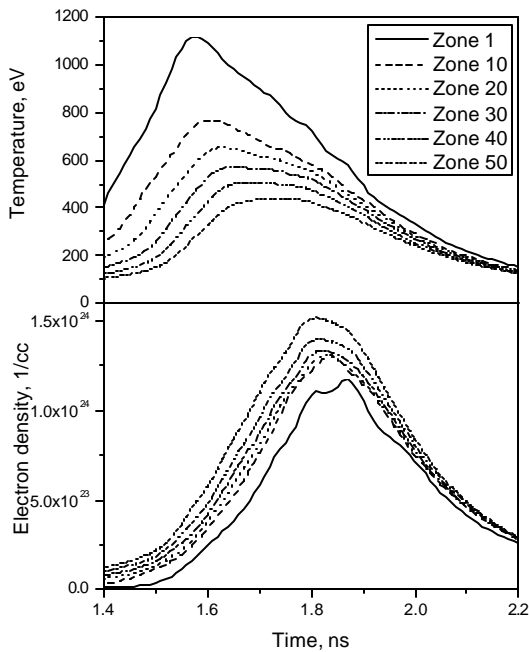


Figure 2. Imploding core electron temperature and density evolution.

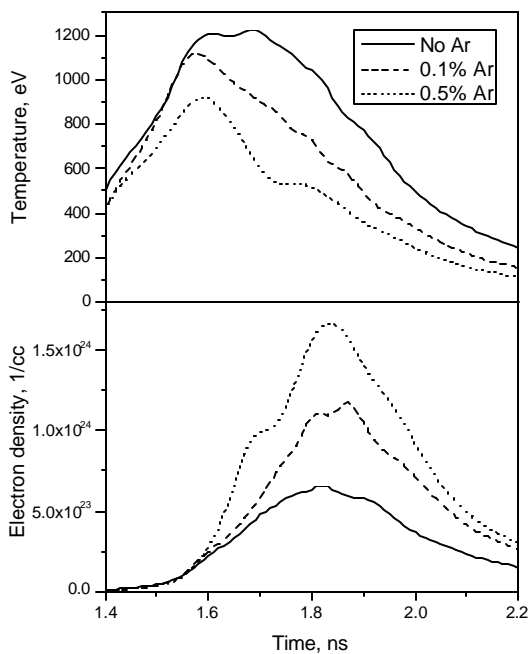


Figure 3. Peak electron temperatures and densities for different concentrations of Ar.

Another important aspect of the calculations is the quality of radiative transfer. To this end, we compare the results of the simulations using time-dependent NLTE atomic kinetics and multi-angle short-characteristics radiation transport, LTE atomic kinetics (Figure 4). The calculations were performed for 0.5% Ar concentration. As the figure indicates, LTE approximation significantly overestimates amount of cooling. Most of the difference in temperature is seen at the relatively hot under-dense stage prior to the stagnation. As the density rises, LTE gains validity. Both of these calculations included high quality radiation transport, so one can expect even greater discrepancy if the diffusion approximation with LTE opacity tables is used for these systems.

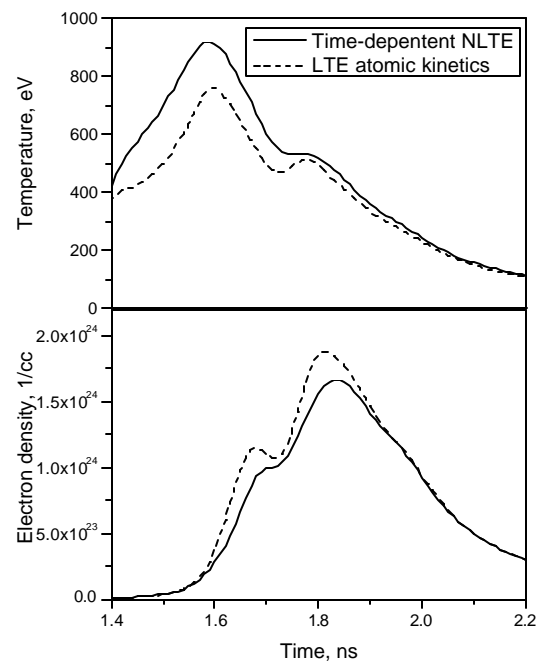


Figure 4. Peak electron temperatures and densities for the calculations with atomic kinetics models.

Lastly, we consider the effects of time-dependent atomic kinetics on ionization distributions and the formation of spectra. To simplify the interpretation of the results, we study uniform plasmas with temperatures and densities relevant for plasma conditions at the different stages of implosion. For this study, we performed two calculations using a single-cell spectral code *PrismSPECT*. All simulations start with LTE populations at the given plasma conditions, and then evolve to steady-state NLTE. We allow the systems to run for 1 ns, with a time grid linearly spaced on a log scale. One run at an electron temperature of 1 keV, and an electron density of

$5.0 \times 10^{23} \text{ cm}^{-3}$ represents plasma conditions at the time of collapse of the main shock wave. The other, at 500 eV and $1.5 \times 10^{24} \text{ cm}^{-3}$ is comparable to the stagnation phase. Figures 5 and 6 illustrate our findings.

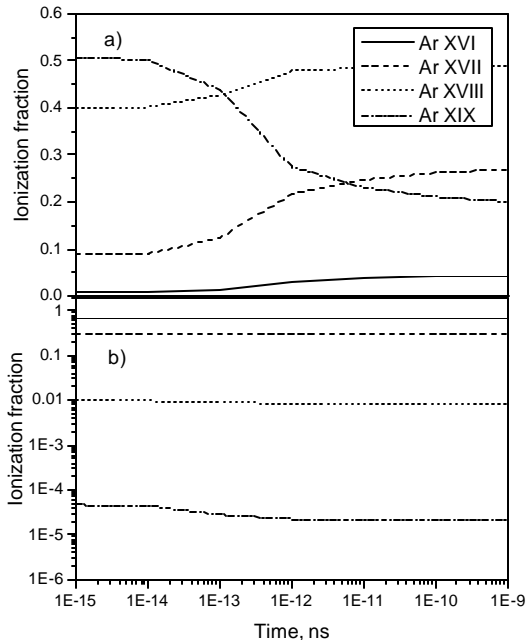


Figure 5. Time-dependent ionization fractions of Ar XVI–Ar XIX. a) $T_e = 1000 \text{ eV}$, $N_e = 5.0 \times 10^{23} \text{ cm}^{-3}$ b) $T_e = 500 \text{ eV}$, $N_e = 1.5 \times 10^{24} \text{ cm}^{-3}$.

At a relatively low density and high temperature, the deviation from LTE is significant (Figure 5a). It takes on the order of a few tens of picoseconds for the populations to reach equilibrium NLTE values. Consequently, the emerging spectra exhibit the evolution of the populations (Figure 6).

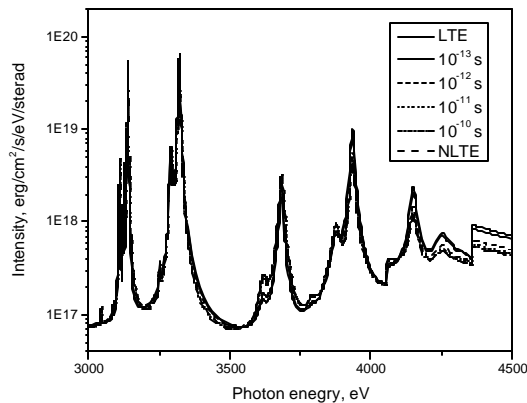


Figure 6. Time evolution of Ar H-shell spectra $T_e = 1000 \text{ eV}$, $N_e = 5.0 \times 10^{23} \text{ cm}^{-3}$.

At the higher density and lower temperature the LTE approximation is valid, and small changes in populations occur on a sub-picosecond scale (Figure 5b). LTE and NLTE spectra are almost indistinguishable.

III. CONCLUSIONS

We have performed simulations of indirectly driven implosions. We have used a 1-dimensional lagrangian radiation-hydrodynamics code *HELIOS* that includes inline collisional-radiative atomic kinetics and multi-angle short-characteristics radiation transport. Driven with a realistic radiation flux, the hydrodynamic simulations compute temperature and density distributions of the imploded core that agree well with the experiment. We have shown that time-dependent atomic kinetics effects are of importance at some stages of the implosion. A more comprehensive study of this subject for NIF size targets will be published elsewhere.

REFERENCES

1. L.A. WELSER et al; Review of Scientific Instruments **74**, p.1921 (2003)
2. L.A. WELSER; Master Thesis, University of Nevada Reno (2003)
3. J.J. MACFARLANE; JQSRT **81**, p. 287 (2003)
4. C.D. DECKER et al; PRL **79**, p. 1491 (1997)
5. I.E. GOLOVKIN et al; PRL **88**, 4, 045002 (2002)
6. L.A. WELSER et al; *in preparation*